Designing, fabrication and characterization of nanostructured functionally graded HAp/BCP ceramics

Smilja Marković[1,*], Miodrag J. Lukić[1], Srečo Davor Škapin[2], Boban Stojanović[3], and Dragan Uskoković[1]

[1] *Centre for Fine Particles Processing and Nanotechnologies, Institute of Technical Sciences of the Serbian Academy of Sciences and Arts, Knez Mihailova 35/IV, 11000 Belgrade, Serbia*

[2] *Advanced Materials Department, Jožef Stefan Institute, Jamova 39, 1000 Ljubljana, Slovenia*

[3] *Faculty of Science, University of Kragujevac, Serbia*

Abstract: Nanostructured calcium phosphate functionally graded materials (FGMs) with simultaneous gradients of density, phase composition, and mechanical properties were fabricated by consecutive uniaxial pressing of stoichiometric (SHAp) and calcium deficient (CDHAp) hydroxyapatite powders in multilayered samples and reaction sintering. During sintering procedure SHAp composition remained stable (HAp) while CDHAp was phase transformed in biphasic calcium phosphate (BCP, i.e. HAp+β-TCP) yielding HAp/BCP FGMs. To reduce mismatch stress between adjacent layers, generated during sintering, gradient of phase composition was optimized by introducing intermediate layer(s) made from mixture of SHAp and CDHAp in appropriate mass ratio. Optimal processing conditions for preparation of nanostructured ceramics were provided *via* two-step sintering. High-quality FGMs structure, without delamination, cracks and micro-structural damages was observed by SEM technique; moreover, a detailed examination by FE–SEM established the unidirectional (perpendicular with respect to the layers) gradual change of microstructure, from fully dense to ~ 40% of porosity. Detailed micro-Raman and FTIR spectroscopy studies showed increase of β-TCP amount along the FGMs height, confirming gradient of phase composition. Mechanical

properties measured by microindentation revealed gradual change of microhardness from 650 to 115 HV, with simultaneous change of Young's modulus from 92 to 24 GPa.

Keywords: Sintering; Functionally graded materials; Calcium phosphates; Nanostructure; Mechanical properties.

***Corresponding Author**

Smilja Marković

Senior Research Associate

Centre for Fine Particles Processing and Nanotechnologies, Institute of Technical Sciences of SASA, Knez Mihailova 35/IV, 11000 Belgrade, Serbia

Tel: +381 11 2636 994

Fax: +381 11 2185 263

e-mail: smilja.markovic@itn.sanu.ac.rs

1. Introduction

Functionally graded materials (FGMs) are defined as materials which possess, continuous or stepped, spatial changes of properties [1–3]. The gradual change of chemical composition, grain size, porosity, etc., could be tailored to produce gradual change of features (electrical, magnetic, biological, etc.) necessary for desired applications of FGMs. After the pioneer works of Japanese scientists on FGMs in the field of thermal barrier coatings and stress relief materials in the aerospace industry [1], this concept has been used for fabrication of various technological components, such as electrical [4,5] and electrochemical devices [6,7], as well as biomaterials [8-10]. Nowadays, functionally graded biomaterials represent an attractive class of materials having properties that cannot be attained in any spatially homogeneous materials [11], such as mechanical strength and biocompatibility, mainly through ceramic/metal [12] and ceramic/polymer FGMs [13]. Besides, ceramic/ceramic functionally graded biomaterials exhibit the advantage over substrate coatings in interfacial bonding quality and reduced thermal stresses during sintering [14].

Functionally graded biomaterials possess a remarkable potential to establish hierarchical structure similar to that in bone [10]. Suchanek and Yoshimura [15] reviewed the hierarchical structure of the bone: outer compact layer is dense with high mechanical strength (cortical bone); inner layer is porous (cancellous bone), allowing cells proliferation and vascularization, while in the core is bone marrow. Some of the important aspects in designing successful implant materials are creating stable interface and matching of mechanical properties with host tissue [16,17]. In the field of bone tissue reconstruction, in spite of their poor osteoinductive properties and brittle nature, calcium phosphate materials, which are compositionally similar to bone mineral, biocompatible, bioactive, and osteoconductive, still represent the most promising materials for bone grafting [18]. Mostly used calcium phosphate materials are hydroxyapatite (HAp), beta-tricalcium phosphate (β-TCP), alpha-tricalcium phosphate (α-TCP) and biphasic calcium phosphate (BCP), which is a mixture of either β-TCP and HAp or α-TCP and HAp

[19]. It is known that HAp ceramics directly bond with bone tissue while β-TCP dissolves gradually leaving the place for new bone formation [8]. Concerning the issue of implant resorption rate requirements [20], the advantages of FGMs are possibility to tailor bioactive/bioresorbable bulk implant materials [21] through the combination of HAp and β-TCP [22]. The spatial gradient of phase composition, from BCP with different HAp/β-TCP ratio to pure HAp provides better environment for bone formation and osteoitegration [23]. Such prepared HAp/BCP FGM will make available direct bonding of HAp surface to bone tissue while BCP surface with appropriate HAp/β-TCP ratio would dissolve to supply calcium and phosphate for a new bone growth. Finally, the possibility to tailor certain level of porosity in the bulk calcium phosphate ceramics is especially important for enhanced transport of biologically important species such as fibrinogen, insulin and type I collagen, as well as for adsorption of proteins [24]. The role of microporosity is also important in macroporous scaffolds for improved growth factor retention [25], to control bioactivity and accelerate osteointegration [26].

Until now, gradient of properties in FGMs was produced with techniques such as: chemical and physical vapor deposition, reaction sintering, plasma spray, casting processes, laser cladding, bionics technique, self-propagating high-temperature synthesis, etc [5,27-32]. Among mentioned, powder processing is the simplest method for producing ceramic components and frequently used since simplicity of the overall process is usually highly demanded. FGMs could be green shaped by successive uniaxial pressing of powders [5,27,28], while subsequent densification results in formation of FGM components. Sintering of FGM is the most challenging step within the powder processing, since the different constituents of FGM usually shrink with different rates and the resulting mismatch stresses can lead to warping, cracking or delamination of the material [27,33]. To obtain high-quality FGMs with desired grain size and density, free from any form of deformation, it is desirable to know densification kinetics of every graded layer in FGM and to design sintering strategy.

Continuing our previous studies on fabrication of dense nanostructured hydroxyapatite [34], and calcium deficient hydroxyapatite [35] ceramics, here, we deal with their combination in the aim to prepare FGM with unique properties. The idea of this study was to establish a model system for engineering of nanostructured calcium phosphate sintered ceramics with simultaneous spatial gradients of microstructure (density), phase composition (HAp/β-TCP ratio), and mechanical properties (hardness and Young's modulus). An important processing goal was to obtain high-quality materials without macro- and micro-structural damages. To solve significant fabrication problem, induced by mismatch stress, compositional gradient was optimized. Three- and five-layered SHAp/CDHAp samples with different compositional gradient were fabricated by the powder-stacking method and uniaxially pressing process. Two-step sintering (TSS) method was used to convert multilayered samples to nanostructured FGMs.

2. Materials and methods

2.1 Starting powders

According to our previous investigations, two calcium phosphate powders, stoichiometric (SHAp) and calcium deficient (CDHAp) hydroxyapatite, were chosen for the preparation of HAp/BCP FGMs.

The SHAp and CDHAp powders were prepared by hydrothermal processing of chemically precipitated material. The ratio of Ca/P was adjusted to be 1.67 and 1.63 for SHAp and CDHAp, respectively. The solution of calcium ions was made by dissolving of $Ca(NO_3)_2 \cdot 4H_2O$ in distilled water. The phosphate solution was made by dissolving 85% H_3PO_4 in distilled H_2O, and 25% NH_4OH was added to both of these solutions to provide stable pH of 11. Supersaturated solution of Ca^{2+} ions was drop-wise added in the phosphate solutions. The obtained suspensions were hydrothermally processed in stainless-steel reactor on 200 °C under the pressure of 2 MPa and stirring of 400 rpm. Afterward, the autoclave was quenched down to room temperature. The precipitate was washed out to pH 7 with distilled water to remove

residual ions. After filtering, the filter cake was dried in oven at 80 °C during 18 h, and grounded to obtain the powdered materials [34–36]. Phase composition of the powders was determined using a powder X-ray diffractometer (Philips PW 1050; Almelo, The Netherlands). The particle size distribution was measured by the laser light-scattering particle size analyzer (PSA) (Mastersizer 2000; Malvern Instruments Ltd., Malvern, Worcestershire, U.K.). The powders' specific surface area (SSA) was measured by standard Brunauer–Emmett–Teller (BET) technique with N_2 adsorption–desorption isotherms at −195.8 °C (Gemini 2370 V5, GA; Micromeritics, Norcross, GA). Primary particle size and morphology were investigated by transmission electron microscope (TEM; JEOL 2100, Tokyo, Japan), and field emission scanning electron microscope (FE–SEM, Supra 35 VP; Carl Zeiss, Oberkochen, Germany) equipped with energy dispersive spectrometer (Inca 400; Oxford Instruments, Abingdon, U.K.).

2.2 Designing and sintering of FGMs

At first, to estimate average green density of SHAp and CDHAp used for the preparation of the graded layers in FGMs, the monomorph layers were pressed in the same conditions as FGMs. According to Archimedes' principle, the values of 55 and 53.5 % of theoretical density (T.D.; T.D. for HAp = 3.16 g/cm^3) were estimated for SHAp and CDHAp, respectively. Furthermore, in order to determine their densification behavior, initial powders were sintered in a heating microscope with automatic image analysis (HT-19; Hesse Instruments, Osterode am Harz, Germany). The sintering shrinkage of uniaxially pressed (P = 150 MPa) cylindrical compacts (∅ 6 mm and $h \approx 3$ mm) was recorded in radial (d) direction at time intervals of 2 sec during the experiments. The non-isothermal experiments were performed in air to 1200 °C, with heating rates of 2, 5, 10 and 20 °C/min.

The HAp/BCP FGMs were fabricated by: (1) powders stacking and uniaxially pressing, and successive (2) sintering. At the start, a bilayered cylindrical compact consisting of CDHAp layer on the top of SHAp layer was fabricated. A die (∅ 6 mm) was filled with 73.5 mg of

SHAp powder. The punch was then placed in the die and tapped; in the next step the punch was removed from the die and filled with 73.5 mg of CDHAp powder. The punch was put back in the die and sample was uniaxially pressed into cylindrical compacts under a pressure of 150 MPa along the thickness direction of the layers. In the following, mixtures of SHAp and CDHAp powders, corresponding to 20 wt% SHAp–80 wt% CDHAp (denoted 20:80), 50 wt% SHAp–50 wt% CDHAp (denoted 50:50), and 80 wt% SHAp–20 wt% CDHAp (denoted 80:20), were homogenized and used to produce three- and five-layered FGMs. Design of layers in uniaxially pressed green pellets and description of the layers phase composition were schematically presented in Fig. 1. In all cases, chemical composition was changed from SHAp to CDHAp, but with different SHAp/CDHAp ratios. The thickness of each layer was about 800 μm. In the next phase, multilayered green pellets were transformed in FGMs by two-step sintering (TSS) process. TSS was performed in a tube furnace; the samples were heated to 900 °C (T_1) and after retention for 5 min were cooled down to 850 °C (T_2) and kept for 20 h. The heating rate was 2 °C/min while cooling rate between T_1 and T_2 was 50 °C/min. After T_2, samples were naturally cooled down with the furnace to room temperature. TSS conditions for preparation of nanostructured calcium phosphate ceramics were established previously [34]. Hereafter, FGMs prepared by sintering of two-, three- and five-layered pellets are referred as FGM-2, FGM-3 and FGM-5, respectively.

To calculate the residual stresses and predict distortions that could occur during sintering of bilayered sample (FGM-2) a finite element analysis (FEA) using PAK finite element solver [37] was performed. The linear coefficients of thermal expansion (CTE), calculated from the shrinkage data for SHAp and CDHAp, were used as input data for FEA; modeling was done for data recorded at 970 °C, where densification mismatch is the largest.

2.3 Characterization of FGMs

To examine the gradient of microstructure using the FE−SEM, samples were grinded perpendicularly with respect to the layers; the cross−sections were polished, thermally etched (at 750 °C for 10 min), and afterwards carbon coated. The FE−SEM micrographs were recorded at 200 x 200 μm vertical area steps to gain an insight into the whole graded profile. The recorded micrographs were used for estimation of the average grain size by measuring the largest diagonal of more than 200 grains with a SemAfore digital slow scan image recording system (version 4.01 demo; JEOL, Tokyo, Japan). A scanning electron microscope (SEM, JEOL JXA 840A) was used to observe FGMs' architectures.

The gradient of phase composition was studied by vibrational spectroscopy techniques. Micro-Raman spectroscopy was performed using a DXR Raman microscope (Thermo Scientific, Madison, WI, USA). The 532 nm line of a diode-pumped solid-state high-brightness laser was used as the excitation source. The Raman spectra were recorded in the frequency interval of 3500–100 cm^{-1}, with a resolution of 4 cm^{-1}. Fourier Transformed Infrared (FTIR) measurements were carried out on Perkin Elmer Spectrum 100 FTIR spectrophotometer coupled to a Spotlight FTIR microscope equipped with nitrogen cooled MCT detector. The FTIR spectra were recorded in the frequency interval of 2000–500 cm^{-1}, with a resolution of 2 cm^{-1}. The vibrational spectra were taken on the polished cross−sectional surfaces, at 100 x 100 μm area and 800 μm vertical line steps. The deconvolution of the recorded Raman and FTIR spectra was done using *PeakFit*™ software [38]. Before fitting, for the sake of comparison, investigated peaks area was normalized to 1. The Gaussian, Lorentzian, Voight and Pearson function were tested, finally, the Voight line shape was chosen for the fitting. The iteration cycles of fitting procedure were repeated to get the best coefficient of determination, r^2 (the best value of r^2 is 1.0). Initial deconvolution procedure was carried out for the FGM segment with nominally the highest amount of β-TCP.

The gradient of mechanical properties was studied by Vickers microhardness test using a Fischerscope H100C (Helmut Fischer, Sindelfingen-Maichingen, Germany). The microhardness and Young's modulus were measured as function of microstructural changes in FGMs at 200 μm vertical line steps; applied load was 1 N (100 g) for 5 seconds. Each measurement was done three times to evaluate an average microhardness and Young's modulus values.

3. Results and discussion

3.1 Characteristics of starting powders

A detailed characterization of SHAp and CDHAp powders was the subject of our previous papers [34–36]. Here, we point out the powders' properties: phase composition, degree of crystallinity, particle size distribution, stoichiometry, morphology and specific surface area, which influenced sinterability and consequently the quality of the FGMs.

Analysis of XRD data, Fig. 2, shows that SHAp and CDHAp powders are pure hydroxyapatite phase (JCPDS 09-0432), with crystallinity degree of 62 and 73 %, respectively. Morphology analyses, FE–SEM and TEM, as well particle size distribution, prove that SHAp and CDHAp powders have uniform nanosized particles, with neglecting agglomeration. EDS measurements reveal Ca/P ratio of 1.67 and 1.63 for SHAp and CDHAp, respectively. Additionally, BET analysis of the SHAp and CDHAp nanopowders shows a relatively large SSA value of 49.5 m^2/g. According to these characteristics, both powders are particularly suitable for sintering. The main characteristics of the starting powders are summarized in Table 1.

3.2 Designing of FGMs and sintering

It is known that during sintering of multilayered samples, the adjacent layers should have the same or similar densification behavior in order to reduce mismatch stresses during the heating and cooling cycles [27,33]. Besides, stoichiometry (Ca/P ratio) of calcium phosphate powders has great impact on densification kinetics [39]. Thus, before designing of FGMs, densification behavior of SHAp and CDHAp starting powders was examined to find whether they are compatible for the preparation of FGMs without macro- and micro-structural failures.

The percentage of shrinkage was calculated from experimental data recorded in radial (d) direction and using Eq. (1):

$$shrinkage\ \ (\%) = \frac{\Delta d}{d_o} \times 100 \tag{1}$$

where Δd denotes the difference between the initial value of diameter d_o (at time t_o) and the values of d_i (at time t_i). Assuming isotropic shrinkage of the pellets, the instantaneous density (ρ_i) during sintering was calculated from the shrinkage data ($\Delta d/d_o$) using Eq. (2) [40,41]:

$$\rho_i = [1/(1 - \Delta d/d_o)]^3 \rho_o \ \text{ i.e. } \ \rho_i = (d_o/d_i)^3 \rho_o \tag{2}$$

where ρ_o is the density of a green pellet.

Fig. 4 shows density *vs*. temperature for SHAp and CDHAp specimens non-isothermally sintered to 1200 °C with heating rates of 2, 5, 10 and 20 °C/min. Obviously, regardless the heating rate, there is always a difference in densification behavior between SHAp and CDHAp. Generally, densification behavior depends on phase composition, green density, temperature, time, atmosphere, etc. [40]. Here, the different densification of SHAp and CDHAp primary depends on stoichiometry effects. It can be noticed that the densification curves of SHAp have similar shape with modest but systematic dependence on the heating rate; actually, with the increase of heating rate, the temperature at which densification begins is shifted toward higher temperatures. The main densification of SHAp occurs in the temperature interval 700–950 °C, while the further increase of temperature provoke grain growth. Densification curves

for CDHAp exhibit very different behavior than those for SHAp: (1) the densification starts around 800 °C and does not finish to 1200 °C, (2) the beginning of densification is shifted to the lower temperatures with faster heating; also, the faster heating results in higher densification. The unusual behavior that increased heating rate increases densification has been explained by two processes: (1) β-TCP formation kinetics, which occur during heating and hinders densification, and (2) influence of surface diffusion of CDHAp system [36,39,42]. Furthermore, previously has been found that amount of TCP phase, representing the sum of β- and α-TCP, exponentially increase with the decrease of heating rate [36].

The von Mises stresses were used as the key indicators to determine stress levels and evaluate the stress distribution in FGM-2. Fig. 5(a) shows linear CTE vs. temperature for SHAp and CDHAp samples; CTE data are calculated from the shrinkage data recorded during heating by 10 °/min. Fig. 5(b) presents the von Mises stress distribution for FGM-2 ceramic at 970 °C calculated by FEA. Numerical results show that the von Mises stress varies from 170 MPa to 9.7 GPa. The highest von Mises stresses are located at the interface between the layers, with the values of 5 GPa in its center and even to 10 GPa on the outer surface (Fig. 5(b)). Thus, deterioration of the FGM-2 structure could be expected due to the large stress developed at adjacent layers interface during the sintering. To prove the theoretical prediction, FGM-2 was sintered up 1200 °C with a heating rate of 10 °C/min. Photographs, recorded during sintering in heating microscope, show the start of the sample deformation at 968 °C (Fig. 5(c)) which is in accordance with the data of the linear CTE. Macrostructural failure is confirmed by SEM of FGM-2 cross-section; large crack is shown to develop at the layers interface area inducing a delamination (Fig. 5(d)).

To reduce densification mismatch between adjacent layers, gradient of phase composition was optimized. The intermediate layers of SHAp and CDHAp mixture were introduced between SHAp and CDHAp layers; thus, instead bilayered SHAp/CDHAp, three- and five-layered pellets with graded change in phase composition were prepared, as it is shown in Fig. 1. Besides, in the aim to produce nanostructured FGMs, instead of conventional

sintering, TSS was applied. The TSS conditions were determined previously [34], while, the heating rate of 2 °/min was chosen since the fact that yields the largest amount of TCP produced by CDHAp phase transformation [36].

3.3 Gradient of microstructure

SEM micrograph of FGM-3 cross-section surface is presented in Fig. 6(d); the profile is segmented and labeled as bottom, middle and top part. The SEM micrograph confirms high-quality of whole FGM-3 specimen; there is no delamination, excessive shape distortion, cracks and micro-structural damages developed during TSS, grinding and polishing processes. FGM-3 is characterized by a continual change of microstructure from the bottom part to the top; there is no apparent interfacial region or residual porosity. It should be emphasized that the intermediate layer of SHAp and CDHAp powders mixture (50:50), introduced in the green sample, diminished mismatch stress and provided excellent sinterability.

The microstructural gradient of FGM-3 is confirmed by FE–SEM. Fig. 6 (a-c) shows FE–SEM images of the central parts of the graded layers and corresponding grain size distributions. In the FGM-3 bottom part, made of SHAp, fully dense material with significant microstructural uniformity can be observed. According to the grain size distribution, the largest number of grains is in the range from 60 to 70 nm with the average size of 68.4 nm. In the FGM-3 middle part, mixing of equal amounts of SHAp and CDHAp powders yielded to the negligible modification in microstructure. Achieved relative density is about 90 %, with small fraction of remaining porosity implying that overall sinterability of the middle graded layer is dominantly influenced by the SHAp nanopowder. The grain size distribution shows a slight non-uniformity: nanometer-sized grains are the main fraction, however, minor number of grains significantly exceeding nanometer range is observed. Actually, the majority of grains are in the range from 40 to 50 nm, while the average size is 62.7 nm. The appearance of larger and smaller grains in the FGM-3 middle part can be considered from the point of view of sintering

processes at the SHAp and CDHAp particles' boundaries because of different sintering mechanisms [34,42]. In the FGM-3 top part, prepared of CDHAp, porosity of about 40 % can be estimated. That is in agreement with density value of 1.9 g/cm^3, calculated according to the shrinkage data for early stage sintering of CDHAp, in temperature range 850–900 °C. Initial nanoparticles could be recognized, with evidently formed interparticles' necks.

Photograph and SEM micrograph of cross-section surface of FGM-5 are shown in Fig. 7 (f-g), confirming high-quality of the sample. The cross-section profile is segmented and labeled as bottom, middle_1, middle_2, middle_3 and top graded layer, which central parts' FE−SEM images and corresponding grain size distributions are presented in Fig. 7 (a-e). As well for the FGM-3, in the FGM-5 sample, gradients of porosity and grain size distribution uniformity are observed. FGM-5 bottom part, prepared of SHAp, has uniform microstructure with the majority of grains in the range from 40 to 60 nm. Existence of 20 wt% of CDHAp in powders mixture used for preparation of middle_1 graded layer resulted in increase of larger grains fraction, while the average size is practically the same for bottom and middle_1 graded layers. Increasing of CDHAp amount to 50 wt. % in powders mixture used for preparation of middle_2 graded layer results in small part of remaining porosity, similar as in the case of FGM-3 corresponding part. Also, grain size distribution is bimodal, with maxima around 55 and 85 nm. Comparing to the FGM-3 sample, the trend is the same, but grains are smaller, with both mean values in the nanometer range. The average grain size is approximately 75 nm. This could be a consequence of the presence of more graded layers in FGM material and more discrete step changes in properties along FGM. Further increase of amount of CDHAp powder in green layers causes the increase of final porosity. Actually, in the FGM-5 middle_3 graded layer, a large fraction of porosity is observed, with partially sintered regions; furthermore, FGM-5 top part shows only slight densification resulting from interconnection of initial particles through necks formation process in early sintering stage. To produce larger fractional porosity it is necessary to use ≥ 50 wt% of CDHAp in the SHAp/CDHAp powders mixture.

The results of FE–SEM analyses establish stepped gradient of density in nanostructured FGMs.

3.4 Gradient of phase composition

Raman spectroscopy is an excellent characterization tool to identify the phase evolution as a function of HAp stoichiometry, because it is very sensitive to small amounts of other phases. Traces of β-TCP (non-detectable by XRD) in the mixture with HAp yield to the broadening of the *v*1 vibrational mode in the Raman spectrum. Actually, β-TCP crystal structure possesses lower symmetry than HAp; distortion of the PO_4 tetrahedra results in a degeneration of ν1 symmetric stretching mode in the case of β-TCP, thus, two bands appear at 947 and 968 cm^{-1} [43,44]. More precisely, the superposition of ν1 vibrations of pure HAp and β-TCP results in a double-band structure; the band at around 960 cm^{-1} will be broadened at the low frequency side (small shoulder appears between 940 and 950 cm^{-1}) [45,46]. Thus, that was the reason why Raman spectroscopy was chosen to study the gradient of phase composition in HAp/BCP FGMs.

At first, we noticed that Raman spectra of all investigated segments in FGM-3 and FGM-5 samples are almost identical. Thus, for clarity, in this paper, only the micro-Raman spectrum of FGM-5 top segment is presented in the whole recorded spectral range, Fig. 8(a). In all spectra only the typical apatite phosphate (PO_4^{3-}) modes exist at: 431, 450 cm^{-1} (O–P–O doubly degenerated bending mode, ν2); 580, 592, 609 cm^{-1} (O–P–O triply degenerated bending mode, ν4); 964 cm^{-1}(P–O non-degenerated symmetric stretching mode, ν1); and 1029, 1047, and 1078 cm^{-1} (P–O triply degenerated antisymmetric stretching mode, ν3) [47,48]. All observed bands match with those in FT-Raman spectrum of deproteinated human cortical bone [49,50] implicating compositional compatibility between the artificial material and mineral part of natural bone. Furthermore, to find low frequency broadening of the ν1 band and to confirm the existence of β-TCP crystal phase, detailed analysis of 1000–900 cm^{-1}spectral region (Fig.

8(b)) was done; the band was deconvoluted in the PeakFit computing program. Number of the peaks in the deconvoluted spectra was set to three, two of them, at 963 and 955 cm^{-1} were attributed to HAp while peak at 949 cm^{-1} was attributed to β-TCP. The results of fitting include recorded, deconvoluted and calculated lines, also, peaks area (denoted as *a*) in percents (because of space restriction the results of fitting are presented only for bottom, middle and top parts of FGM-5, Fig. 9). The comparison of HAp and β-TCP peaks area ratio in all the examined segments clearly shows that amount of β-TCP gradually increase from the bottom (pure HAp) to the top side, in both the FGMs. The *a* value, changed from 0.04 to 2.49 %, is rather relative than absolute measure of β-TCP.

FTIR technique, complementary to Raman spectroscopy, allows study of structural OH group vibrations during phase evolution from HAp to BCP, even when small amount of β-TCP phase was formed. As it is known, β-TCP has no structural OH groups yielding to vanishing of vibrational band near 630 cm^{-1} [43].

As in the case of Raman study, FTIR spectra of all the segments in FGM-3 and FGM-5 samples are almost identical as the consequence of slight change in spatial chemical composition. Thus, only the FTIR reflectance spectrum of FGM-5 bottom segment is presented in the whole recorded spectral range, Fig. 10(a). In all recorded spectra the typical modes exist at: 575 and 600 cm^{-1} (O–P–O doubly degenerated bending mode, ν4); 630 cm^{-1} (O–H libration); 960 cm^{-1} (P–O non-degenerated symmetric stretching mode, ν1); 1050 and 1095 cm^{-1} (P–O triply degenerated antisymmetric stretching mode, ν3) and 1615 cm^{-1} (bending O–H–O) [43]. To confirm decreases of relative content of structural OH groups, detailed analysis of 650–530 cm^{-1}spectral region (Fig. 10(b)) was done; the bands were deconvoluted. Prior to deconvolution, analyzed spectral area was normalized to 1. Relative amount of structural OH groups was correlated with the area of integrated peak centered at ~ 630 cm^{-1}. Figure 11 represents the results of fitting (recorded, deconvoluted and calculated lines, also, the ratio of OH and total integrated peak areas denoted as a_{OH}/a_{sum}) for bottom, middle and top parts of FGM-5. It could

be seen that relative amount of structural OH groups was decreased from the bottom (HAp) to the top (BCP) part of FGM-5.

Both vibrational spectroscopy techniques confirmed formation of HAp/BCP FGMs; (1) Raman spectroscopy determined rises of β-TCP phase, while simultaneously (2) FTIR spectroscopy revealed decreases of relative content of structural OH groups. It should be emphasized that amount of β-TCP is relatively low which is influenced by low sintering temperature, initial powders' stoichiometry and nature of phase transformation. The possibility to vary HAp/β-TCP ratio through FGMs is useful for optimization of dissolution behavior [51].

3.5 Gradient of mechanical properties

Microhardness and Young's modulus of the FGM-3 and FGM-5 as a function of position, and consequently of microstructure and phase composition are shown in Figs. 12 and 13. For FGM-3, the highest microhardness, about 650 HV, is measured for the bottom part consisted of pure HAp phase, and then stepwisely decreased to 140 HV for the top part, confirming graded profile (Fig. 12). Similar results are obtained for FGM-5 (Fig. 13); the highest microhardness of about 640 HV is measured for the bottom part, which then stepwisely decreases to 115 HV for the top part. The same trend is observed in the change of Young's modulus of these samples. For FGM-3, it varies from 92.5 to 27 GPa (Fig. 12), while for the FGM-5 Young's modulus goes from 68 to 24 GPa (Fig. 13). The change of elastic modulus of the FGMs is in agreement with that of sintered HAp materials obtained at different temperatures [52].

From the presented results for microhardness, it can be concluded that the HV values for the bottom and the top graded layers are almost the same for both FGMs, independent on number of the graded layers and phase compositions in the middle. However, it should be noticed that, although the values of mechanical properties are nearly the same, the gradient is more continual for FGM-5. This is easily observable if FGM-3 middle and FGM-5 middle_2 graded layers, having the same starting phase composition, are compared. In the former one, Vickers microhardness varies from 450 to 150 HV from bottom to the top, while in the latter

one, it is in a narrow range from 150 to 100 HV. Thus, the gradient of mechanical properties could be tailored by changing the number of the layers, their thickness, and the gradient of the phase composition i.e. amount of β-TCP crystal phase. The gradient of mechanical properties is influenced by gradients of porosity and β-TCP amount in the bottom-top direction. The obtained gradient of mechanical properties of the FGMs is significant from the point of approaching to that of cortical bone. Numerous studies showed that elastic modulus of approximately 30 GPa is a threshold point where mechanical response of cortical bone and dense sintered calcium phosphates should match [15,53,54]. However, mechanical properties of calcium phosphates are influenced by many parameters, among which porosity has a dominant role [55]. For HAp, elastic modulus is in the range from 80 to 110 GPa, while for β-TCP reaches values of 90 GPa [16,56].

In Table 2, the microstructural, compositional and mechanical characteristics of FGM-3 and FGM-5 bottom and top parts are summarized.

This simple method of powders processing, namely, successive uniaxially pressing and two-step sintering, could be useful for producing of nanostructured HAp/BCP FGMs with appropriate gradients of porosity, phase composition and mechanical properties. These gradients, from stepped to continual, could be tailored by tuning the number of layers and their phase composition. Such FGMs could be used as a model system for overcoming differences in mechanical properties of artificial and natural bone material and finding an optimal level of porosity-controlled bioactivity. After establishing of such a model material, additional improvements could be made; by changing of CDHAp stoichiometry and varying of number and composition of intermediate layers, properties could be precisely tailored. Considering possibilities for continual reconstruction of cancellous bone on the most porous side of the prepared FGMs, macroporous calcium phosphate scaffolds could be fabricated and loaded with some of growth factors with application of appropriate method.

4. Conclusion

It was shown that nanostructured HAp/BCP FGMs with functionally graded chemical and physical properties could be fabricated by powders processing and reaction two-step sintering. The mismatch stress between adjacent layers, generated during sintering, was successfully reduced by optimization of phase composition' gradient; high-quality FGMs, without excessive shape distortion, delamination, development of cracks and micro-structural failures were obtained.

Determined spatial change of porosity, phase composition (HAp/β-TCP ratio) and mechanical properties, with simultaneous enhancement of features promotes fabricated FGMs as functional bioceramics:

(1) The average grain size along the overall FGMs was fairly below 100 nm, approaching dimensionality of HAp crystals in natural bone;

(2) The amount of β-TCP gradually increases along the FGMs height (a possibility to tailor the HAp/β-TCP ratio in FGMs could provide appropriate resorption rate of artificial bone material);

(3) The FGMs mechanical properties approach to that of cortical bone; microhardness was gradually changed from 650 to 115 HV, while Young's modulus graded from 92 to 24 GPa.

Acknowledgements

This study was financially supported by the Ministry of Education and Science of the Republic of Serbia under Grant No. III45004. Part of results was obtained at Jožef Stefan Institute in Ljubljana, Slovenia, owing to the bilateral cooperation program between the Republic of Serbia and the Republic of Slovenia, Grant No. 451-03-1251/2012-09/06. The authors are grateful to Prof. Dr. Miloš Mojović from Faculty of Physical Chemistry, University in Belgrade, Belgrade, Serbia, for micro-Raman measurements.

References

[1] M. Koizumi, M. Niino, Overview of FGM research in Japan, MRS Bull. 20 (1995) 19–21 (Special Issue, Functionally Gradient Materials, ed. E. L. Fleitscher).

[2] M. Koizumi, FGM activities in Japan, Composites B 28 (1997) 1–4.

[3] B. Kieback, A. Neubrand, H. Reidel, Processing techniques for functionally graded materials, Mater. Sci. Eng. A 362 (2003) 81–106.

[4] C.C. Wu, M. Khan, W. Moy, Piezoelectric ceramics with functional gradient: a new application in material design, J. Am. Ceram. Soc. 79 (1996) 809–812.

[5] S. Marković, M. Mitrić, N. Cvjetićanin, D. Uskoković, Preparation and properties of $BaTi_{1-x}Sn_xO_3$ multilayered ceramics, J. Eur. Ceram. Soc. 27 (2007) 505–509.

[6] Z. Liu, M.-F. Han, W.-T. Miao, Preparation and characterization of graded cathode $La_{0.6}Sr_{0.4}Co_{0.2}Fe_{0.8}O_{3-\delta}$, J. Power Sources 173 (2007) 837–841.

[7] M. Niino, M. Koizumi, Projected research on high-efficiency energy conversion materials. In: Ilschner B, Cherradi N, editors. Third International Symposium on Structural and Functional Gradient Materials Proceedings of FGM'94. Lausanne, Switzerland: Presses Polytech. Univ. Romandes; 1995. p. 601–605.

[8] M. Kon, K. Ishikawa, Y. Miyamoto, K. Asaoka, Development of calcium phosphate based functional gradient bioceramics, Biomaterials 16 (1995) 709–714.

[9] I. Manjubala, T.S. Sampath Kumar, Effect of TiO_2–Ag_2O additives on the formation of calcium phosphate based functionally graded bioceramics, Biomaterials 21 (2000) 1995–2002.

[10] W. Pompe, H. Worch, M. Epple, W. Friess, M. Gelinsky, P. Greil, U. Hempel, D. Scharnweber, K. Schulte, Functionally graded materials for biomedical applications, Mat. Sci. Eng. A 362 (2003) 40–60.

[11] M. A. F. Afzal, P. Kesarwani, K. M. Reddy, S. Kalmodia, B. Basu, K. Balani, Functionally graded hydroxyapatite-alumina-zirconia biocomposite: Synergy of toughness and biocompatibility, Mat. Sci. Eng. C 32 (2012) 1164–1173.

[12] X. Bai, S. Sandukas, M.R. Appleford, J.L. Ong, A. Rabiei, Deposition and investigation of functionally graded calcium phosphate coatings on titanium, Acta Biomater. 5 (2009) 3563–3572.

[13] C. Liu, Z. Han, J.T. Czernuszka, Gradient collagen/nanohydroxyapatite composite scaffold: Development and characterization, Acta Biomater. 5 (2009) 661–669.

[14] H. Guo, K.A. Khor, Y.C. Boey, X. Miao, Laminated and functionally graded hydroxyapatite/yttria stabilized tetragonal zirconia composites fabricated by spark plasma sintering, Biomaterials 24 (2003) 667–675.

[15] W. Suchanek, M. Yoshimura, Processing and properties of hydroxyapatite-based biomaterials for use as hard tissue replacement implants, J. Mater. Res. 13 (1998) 94–117.

[16] L.L. Hench, Bioceramics, J. Amer. Ceram. Soc. 81 (1998) 1705–1728.

[17] K.E. Tanner, R.N. Downes, W. Bonfield, Clinical applications of hydroxyapatite reinforced materials, Br. Ceram. Trans. 93 (1994) 104–107.

[18] M. Bohner, L. Galea, N. Doebelin, Calcium phosphate bone graft substitutes: Failures and hopes, J. Eur. Ceram. Soc. 32 (2012) 2663–2671.

[19] S.V. Dorozhkin, Bioceramics of calcium orthophosphates, Biomaterials 31 (2010) 1465-1485.

[20] M.E. Elsalanty, D.G. Genecov, Bone grafts in craniofacial surgery, Craniomaxillofac. Trauma Reconstr. 2 (2009) 125–134.

[21] G. Daculsi, Biphasic calcium phosphate concept applied to artificial bone, implant coating and injectable bone substitute, Biomaterials 19 (1998) 1473–1478.

[22] M. Gasik, A. Keski-Honkola, Y. Bilotsky, M. Friman, Development and optimisation of hydroxyapatite–ß-TCP functionally gradated biomaterial, J. Mech. Behav. Biomed. Mater. 30 (2014) 266–273.

[23] S. Katakam, D. Siva Rama Krishna, T.S. Sampath Kumar, Microwave processing of functionally graded bioactive materials, Mat. Lett. 57 (2003) 2716–2721.

[24] X.D. Zhu, H.J. Zhang, H.S. Fan, W. Li, X. D. Zhang, Effect of phase composition and microstructure of calcium phosphate ceramic particles on protein adsorption, Acta Biomater. 6 (2010) 1536–1541.

[25] J.R. Woodard, A.J. Hilldore, S.K. Lan, C.J. Park, A.W. Morgan, J.A.C. Eurell, S.G. Clark, M.B. Wheeler, R.D. Jamison, A.J.W. Johnson, The mechanical properties and osteoconductivity of hydroxyapatite bone scaffolds with multi-scale porosity, Biomaterials 28 (2007) 45–54.

[26] K.A. Hing, B. Annaz, S. Saeed, P.A. Revell, T. Buckland, Microporosity enhances bioactivity of synthetic bone graft substitutes, J. Mater. Sci.: Mater. Med. 16 (2005) 467–475.

[27] S.E. Schoenberg, D.J. Green, A.E. Segall, G.L. Messing, A.S. Grader, P.M. Halleck, Stresses and distortion due to green density gradients during densification, J. Am. Ceram. Soc. 89 (2006) 3027–3033.

[28] S. Marković, Č. Jovalekic, Lj. Veselinović, S. Mentus, D. Uskoković, Electrical properties of barium titanate stannate functionally graded materials, J. Eur. Ceram. Soc. 30 (2010) 1427–1435.

[29] A. Muthutantri, J. Huang, M. Edirisinghe, Novel preparation of graded porous structures for medical engineering, J. R. Soc. Interface 5 (2008) 1459–1467.

[30] Z. Weidong, L. Qibin, Z. Min, W. Xudong, Biocompatibility of a functionally graded bioceramic coating made by wide-band laser cladding. J. Biomed. Mater. Res. A 87 (2008) 429–433.

[31] E. M. M. Ewais, D. H. A. Besisa, Z. I. Zaki, Influence of MgO addition on the properties of new tailored FGZM/A ceramics, Mat. Sci. Eng. A 578 (2013) 197–206.

[32] S. N. S. Jamaludin, F. Mustapha, D. M. Nuruzzaman, S. N. Basri, A review on the fabrication techniques of functionally graded ceramic-metallic materials in advanced composites, Scientific Research and Essays 8 (21) (2013) 828–840.

[33] K. Wua, S. Scheler, H.-S. Park, M. Willert-Porada, Pressureless sintering of ZrO_2–$ZrSiO_4$/NiCr functionally graded materials with a shrinkage matching process, J. Eur. Ceram. Soc. 33 (2013) 1111–1121.

[34] M.J. Lukić, S.D. Škapin, S. Marković, D. Uskoković, Processing route to full dense nanostructured HAp bioceramics: from powder synthesis to sintering, J. Am. Ceram. Soc. 95 (2012) 3394–3402.

[35] M. Lukić, Z. Stojanović, S.D. Škapin, M. Maček-Kržmanc, M. Mitrić, S. Marković, D. Uskoković, Dense fine-grained biphasic calcium phosphate (BCP) bioceramics designed by two-step sintering, J. Eur. Ceram. Soc. 31 (2011) 19–27.

[36] M.J. Lukić, L. Veselinović, Z. Stojanović, M. Maček-Kržmanc, I. Bračko, S.D. Škapin, S. Marković, D. Uskoković, Peculiarities in sintering behavior of Ca-deficient hydroxyapatite nanopowders, Mat. Lett. 68 (2012) 331–335.

[37] M. Kojic, R. Slavkovic, M. Zivkovic, N. Grujovic, PAK—Finite Element Program for Linear and Non-linear Structural Analysis, Mass and Heat Transfer and Biomechanics, Faculty of Mechanical Engineering, University of Kragujevac, 1996.

[38] Peakfite, version 4.0, SPSS Inc., Chicago, IL, USA.

[39] S. Raynaud, E. Champion, D. Bernache-Assollant, Calcium phosphate apatites with variable Ca/P atomic ratio II. Calcination and sintering, Biomaterials 23 (2002) 1073–1080.

[40] R.M. German, Sintering Theory and Practice, John Willey & Sons, INC, New York, Chichester, Brisbane, Toronto, Singapore, 1996.

[41] H. Su, D.L. Johnson, Sintering of alumina in microwave-induced oxygen plasma, J. Am. Ceram. Soc. 79 (1996) 3199-3210.

[42] E. Champion, Sintering of calcium phosphate bioceramics, Acta Biomat. 9 (2013) 5855–5875.

[43] A. Siddharthan, T.S. Sampath Kumar, S.K. Seshadri, Synthesis and characterization of nanocrystalline apatites from eggshells at different Ca/P ratios, Biomed. Mater. 4 (2009) 045010 (9pp).

[44] J.M. Fernández-Pradas, G. Sardin, J.L. Morenza, Inhomogeneity of calcium phosphate coatings deposited by laser ablation at high deposition rate, Appl. Phys. A 76 (2003) 251–256.

[45] G.L. Darimont, B. Gilbert, R. Cloots, Non-destructive evaluation of crystallinity and chemical composition by Raman spectroscopy in hydroxyapatite-coated implants, Mat. Lett. 58 (2003) 71–73.

[46] A. Aminzadeh, S. Shahabi, L.J. Walsh, Raman spectroscopic studies of CO_2 laser-irradiated human dental enamel, Spectrochim. Acta A 55 (1999) 1303–1308.

[47] R. Vani, E.K. Girija, K. Elayaraja, S. Prakash Parthiban, R. Kesavamoorthy, S. Narayana Kalkura, Hydrothermal synthesis of porous triphasic hydroxyapatite/(α and β) tricalcium phosphate, J. Mater. Sci.: Mater. Med. 20 (2009) 43–48.

[48] A. Bertoluzza, G. Bottura, P. Taddei, A. Tinti, M.A. Morelli, Vibrational spectra of controlled-structure hydroxyapatite coatings obtained by the polymeric route, J. Raman. Spectrosc. 27 (1996) 759–764.

[49] R. Smith, I. Rehman, Fourier transform Raman spectroscopic studies of human bone, J. Mater. Sci.: Mater. Med. 5 (1995) 775–778.

[50] A.F. Khan, M. Awais, A.S. Khan, S. Tabassum, A.A. Chaudhry, I. Rehman, Raman spectroscopy of natural bone and synthetic apatites, Appl. Spectrosc. Rev. 48 (2013) 329–355.

[51] P. Rajesh, C.V. Muraleedharan, S. Sureshbabu, M. Komath, H. Varma, Preparation and analysis of chemically gradient functional bioceramic coating formed by pulsed laser deposition, J. Mater. Sci.: Mater. Med. 23 (2012) 339–348.

[52] O. Prokopiev, I. Sevostianov, Dependence of the mechanical properties of sintered hydroxyapatite on the sintering temperature, Mat. Sci. Eng. A 431 (2006) 218–227.

[53] D.T. Reilly, A.H. Burstein, The mechanical properties of cortical bone, J. Bone Joint Surg. Am. 56 (1974) 1001–1022.

[54] J.D. Currey, Effects of differences in mineralization on the mechanical properties of bone, Philos. Trans. R Soc. London, Ser B 304 (1984) 509–518.

[55] F. Pecqueux, F. Tancret, N. Payraudean, J.M. Bouler, Influence of microporosity and macroporosity on the mechanical properties of biphasic calcium phosphates bioceramics: Modeling and experiment, J. Eur. Ceram. Soc. 30 (2010) 819–829.

[56] S. Ramesh, K.L. Aw, R. Tolouei, M. Amiriyan, C.Y. Tan, M. Hamdi, J. Purbolaksono, M.A. Hassan, W.D. Teng, Sintering properties of hydroxyapatite powders prepared using different methods, Ceram. Int. 39 (2013) 111–119.

Figure captions

Fig. 1. Scheme of uniaxially pressed samples consisted of symmetric layers with different compositions.

Fig. 2. XRD patterns of SHAp and CDHAp nanopowders.

Fig. 3. TEM micrographs of SHAp and CDHAp nanopowders (top); and FE−SEM micrographs with inserted particle size distributions of SHAp and CDHAp (bottom).

Fig. 4. Density (g/cm^3) *versus* temperature for SHAp and CDHAp specimens sintered to 1200 °C by heating rates of 2, 5, 10 and 20 °/min.

Fig. 5. (a) Linear coefficient of thermal expansion (CTE) versus temperature for SHAp and CDHAp; (b) the von Mises stress [MPa] distribution through FGM-2; (c) photograph of cylindrical sample as observed in heating microscope at the beginning of sintering procedure (37 °C) and at temperature when deformation starts (968 °C), and (d) SEM image of FGM-2 cross-section.

Fig. 6. (a-c) FE−SEM micrographs of the segments in FGM-3; (d) SEM image of FGM-3 cross−section, and (e-f) grain size distribution.

Fig. 7. (a-e) FE−SEM micrographs of the segments in FGM-5; (f-g) Photograph and SEM image of FGM-5 cross−section, and (h-j) grain size distribution.

Fig. 8. (a) Micro-Raman spectrum of the top segment in FGM-5; and (b) expanded region of υ1 phosphate band.

Fig. 9. Deconvoluted phosphate (υ1) band of the bottom, central and top segments in FGM-5, and data obtained by deconvolution.

Fig. 10. (a) FTIR spectrum of the bottom segment in FGM-5; and (b) expanded 650-530 cm^{-1} region of υ4 phosphate and O-H libration bands.

Fig. 11. Deconvoluted 650-530 cm^{-1} region of υ4 phosphate and O-H libration bands: bottom, central and top segments in FGM-5, and data obtained by deconvolution.

Fig. 12. (left) SEM image of FGM-3 cross-section with microhardness profile, and (right) Young's modulus across section profile.

Fig. 13. (left) SEM image of FGM-5 cross-section with microhardness and compositional profiles, and (right) Young's modulus across section profile.

Table 1. The main **c**haracteristics of SHAp and CDHAp powders.

Powders	SHAp	CDHAp
Formula	$Ca_{10}(PO_4)_6(OH)_2$	$Ca_{10}(PO_4)_6(OH)_2$
Ca/P	1.67	1.63
Crystallinity degree (%)	62	73
$d_{0.1}$ (nm)	35	65
$d_{0.5}$ (nm)	65	90
$d_{0.9}$ (nm)	120	150
span	1.30	0.94
Specific surface area (SSA) (m^2/g)	49.5	49.5
Green density (% T.D.)	55	53.5

Table 2. Characteristics of FGMs.

FGM-3	Bottom layer	Top layer
Phase composition	HAp	BCP (HAp+β-TCP)
Porosity (%)	~ 2	~ 40
Average grain size (nm)	68.4	Interconnected particles
Microhardness (HV)	650	140
Young's modulus (GPa)	92	27
FGM-5	Bottom layer	Top layer
Phase composition	HAp	BCP (HAp+β-TCP)
Porosity (%)	~ 2	~ 40
Average grain size (nm)	64	Interconnected particles
Microhardness (HV)	640	115
Young's modulus (GPa)	68	24

Fig. 1

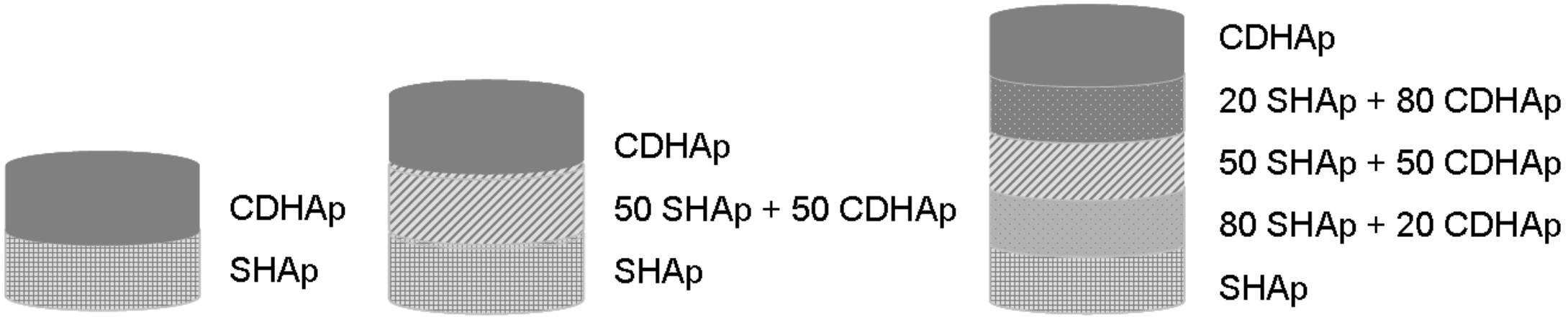
CDHAp
SHAp
CDHAp
50 SHAp + 50 CDHAp
SHAp
CDHAp
20 SHAp + 80 CDHAp
50 SHAp + 50 CDHAp
80 SHAp + 20 CDHAp
SHAp

Fig. 2

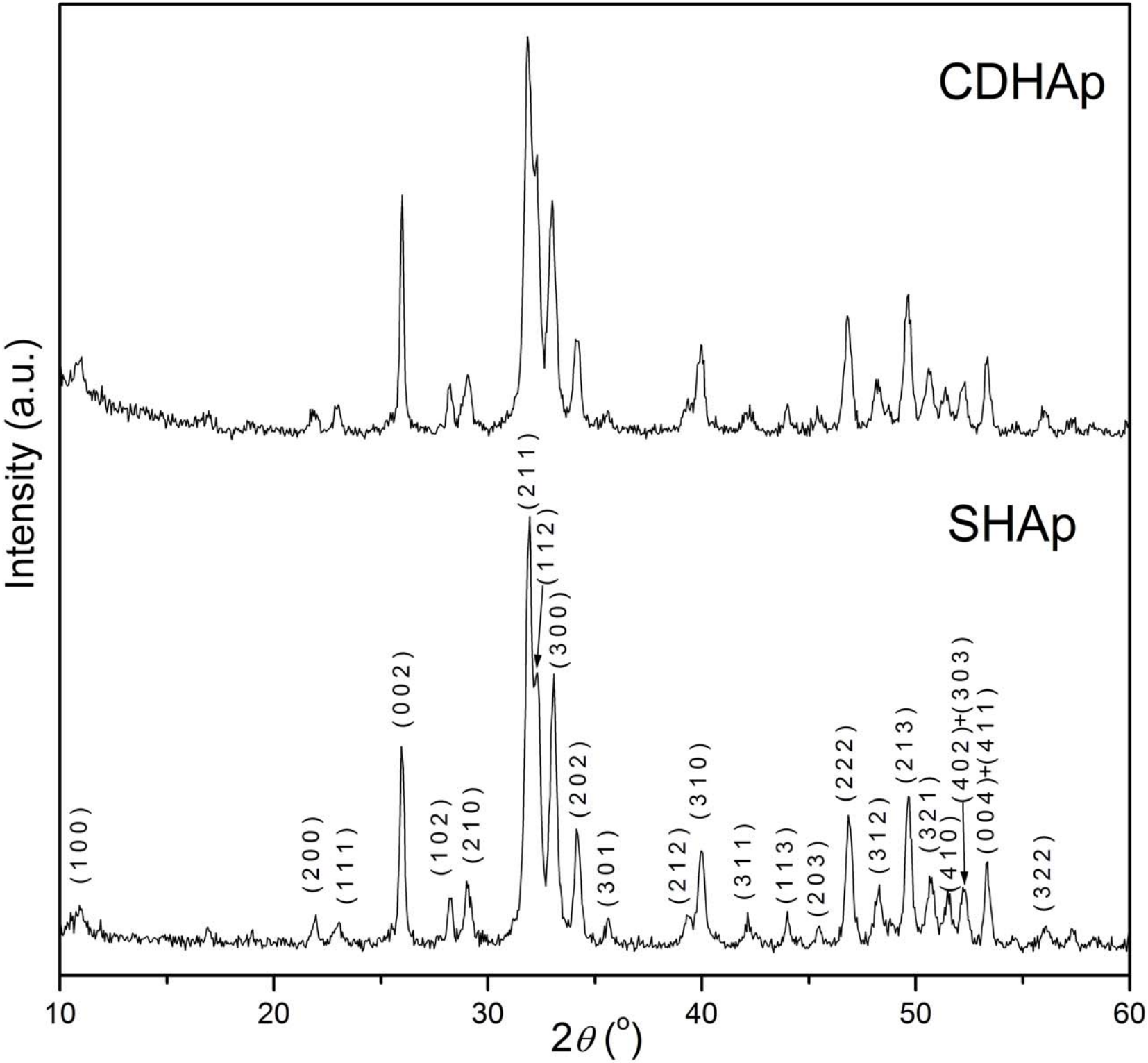
CDHAp
SHAp
Intensity (a.u.)
2θ (°)
10
20
30
40
50
60
(100)
(200)
(111)
(002)
(102)
(210)
(211)
(112)
(300)
(202)
(301)
(212)
(310)
(311)
(113)
(203)
(222)
(312)
(213)
(321)
(410)
(402)+(303)
(004)+(411)
(322)

Fig. 3

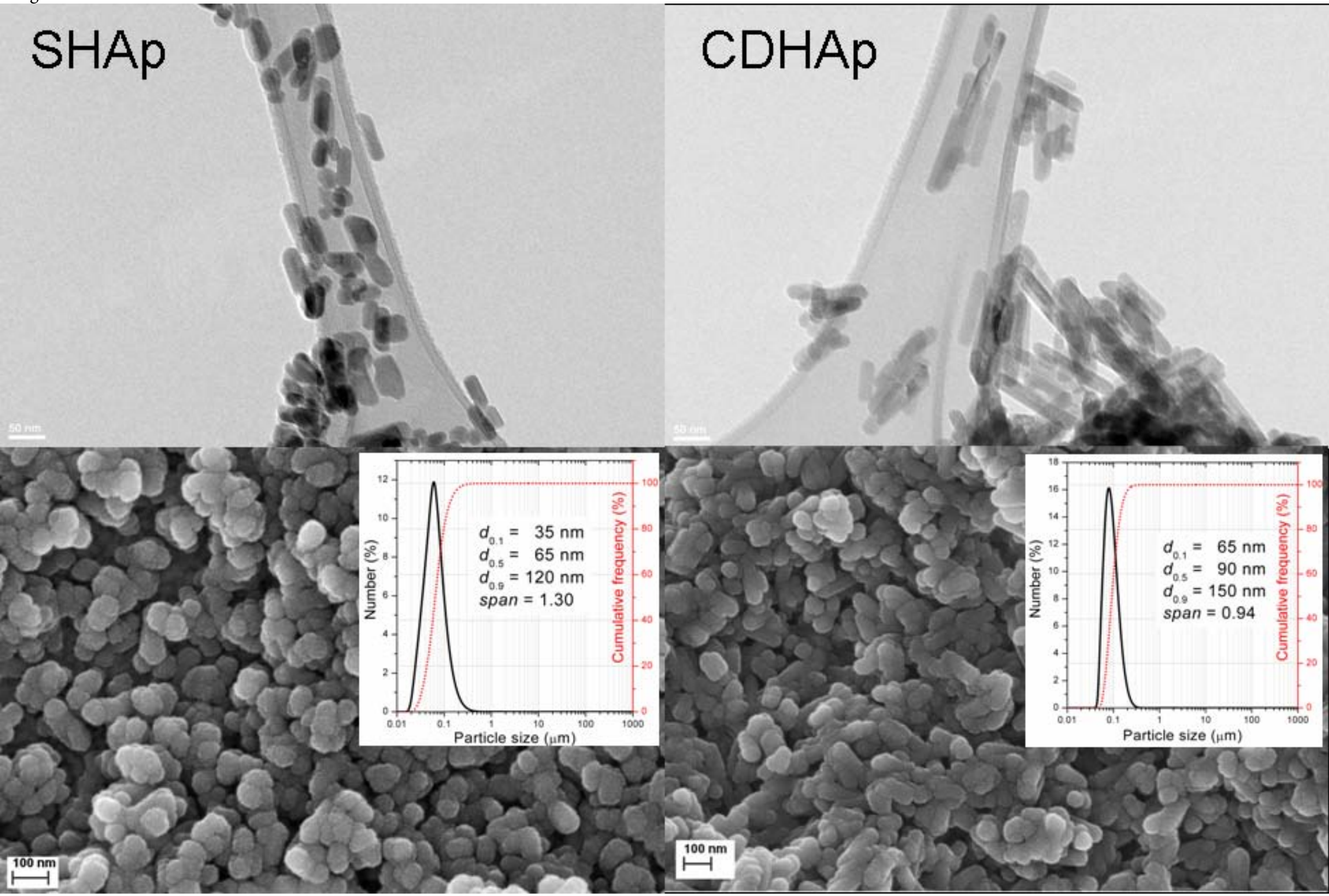
SHAp
CDHAp
50 nm
50 nm
100 nm
100 nm
Number (%)
Cumulative frequency (%)
Particle size (μm)
$d_{0.1}$ = 35 nm
$d_{0.5}$ = 65 nm
$d_{0.9}$ = 120 nm
span = 1.30
$d_{0.1}$ = 65 nm
$d_{0.5}$ = 90 nm
$d_{0.9}$ = 150 nm
span = 0.94

Fig. 4

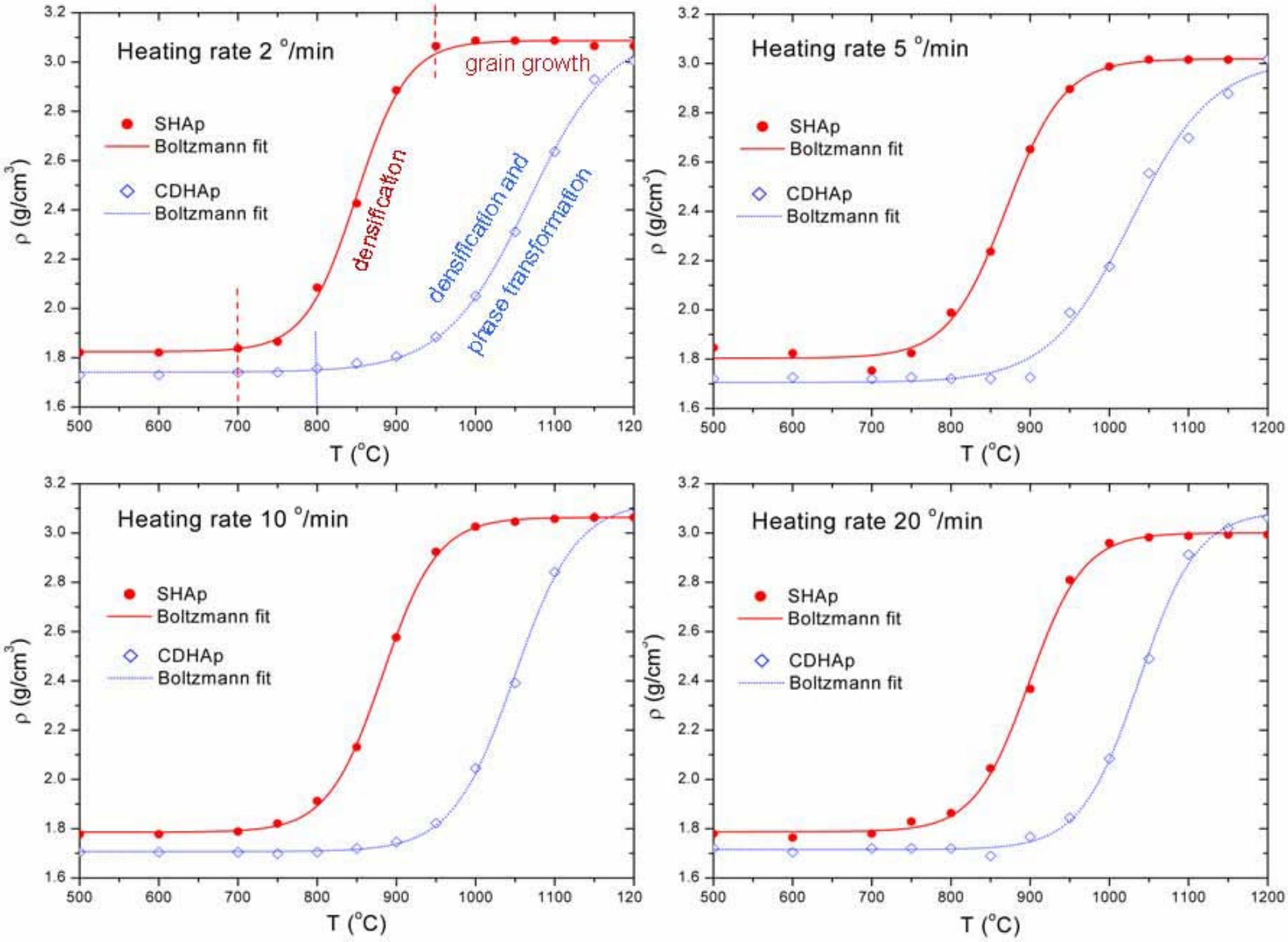
Heating rate 2 °/min
grain growth
densification
densification and
phase transformation
SHAp
Boltzmann fit
CDHAp
Boltzmann fit
ρ (g/cm3)
T (°C)
Heating rate 5 °/min
Heating rate 10 °/min
Heating rate 20 °/min

Fig. 5

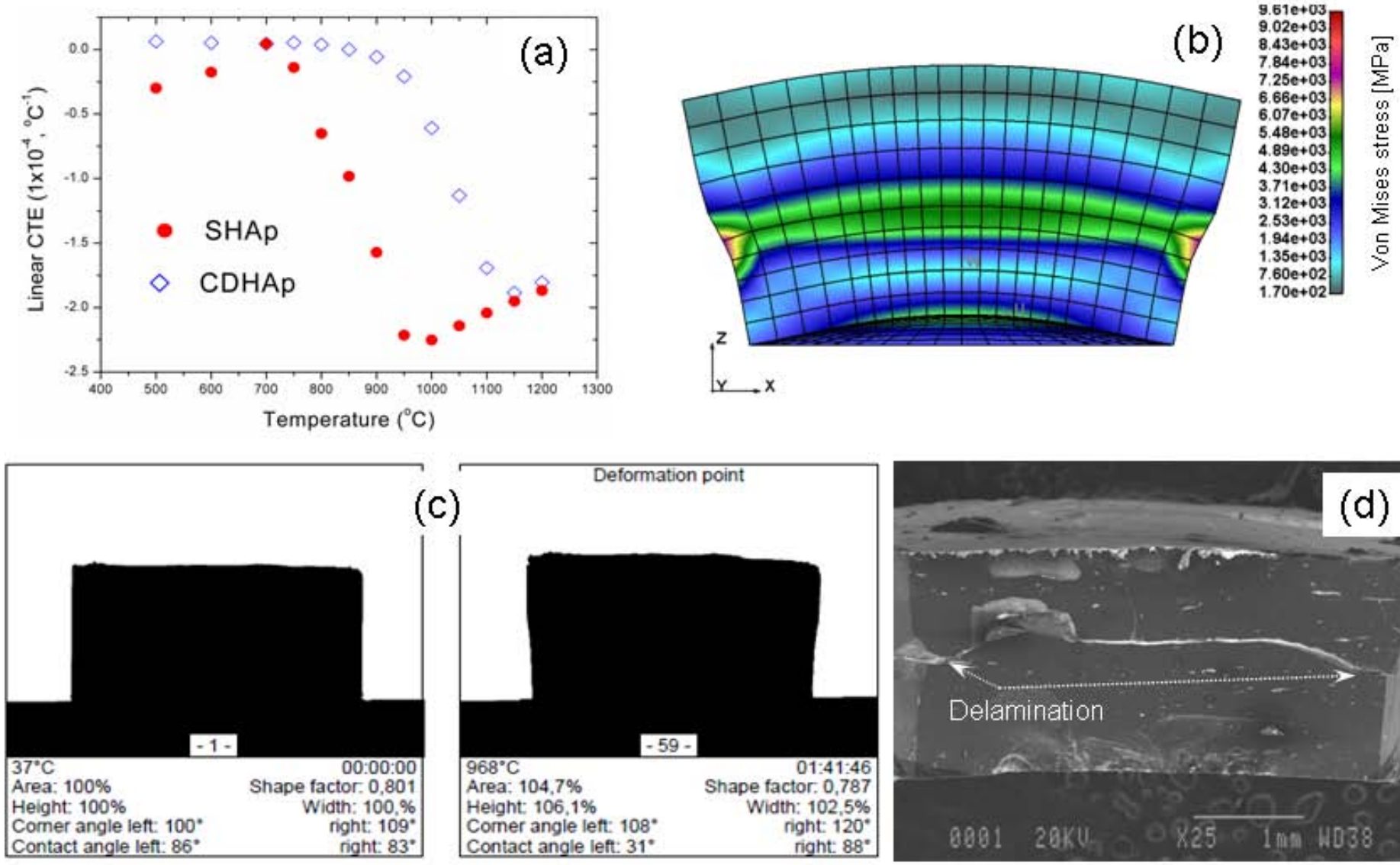
(a)
Linear CTE (1x10^{-4}, °C^{-1})
Temperature (°C)
SHAp
CDHAp
(b)
Von Mises stress [MPa]
9.61e+03
9.02e+03
8.43e+03
7.84e+03
7.25e+03
6.66e+03
6.07e+03
5.48e+03
4.89e+03
4.30e+03
3.71e+03
3.12e+03
2.53e+03
1.94e+03
1.35e+03
7.60e+02
1.70e+02
Z
Y
X
(c)
Deformation point
- 1 -
37°C
00:00:00
Area: 100%
Shape factor: 0,801
Height: 100%
Width: 100,%
Corner angle left: 100°
right: 109°
Contact angle left: 86°
right: 83°
- 59 -
968°C
01:41:46
Area: 104,7%
Shape factor: 0,787
Height: 106,1%
Width: 102,5%
Corner angle left: 108°
right: 120°
Contact angle left: 31°
right: 88°
(d)
Delamination
0001 20KV X25 1mm WD38

Fig. 6

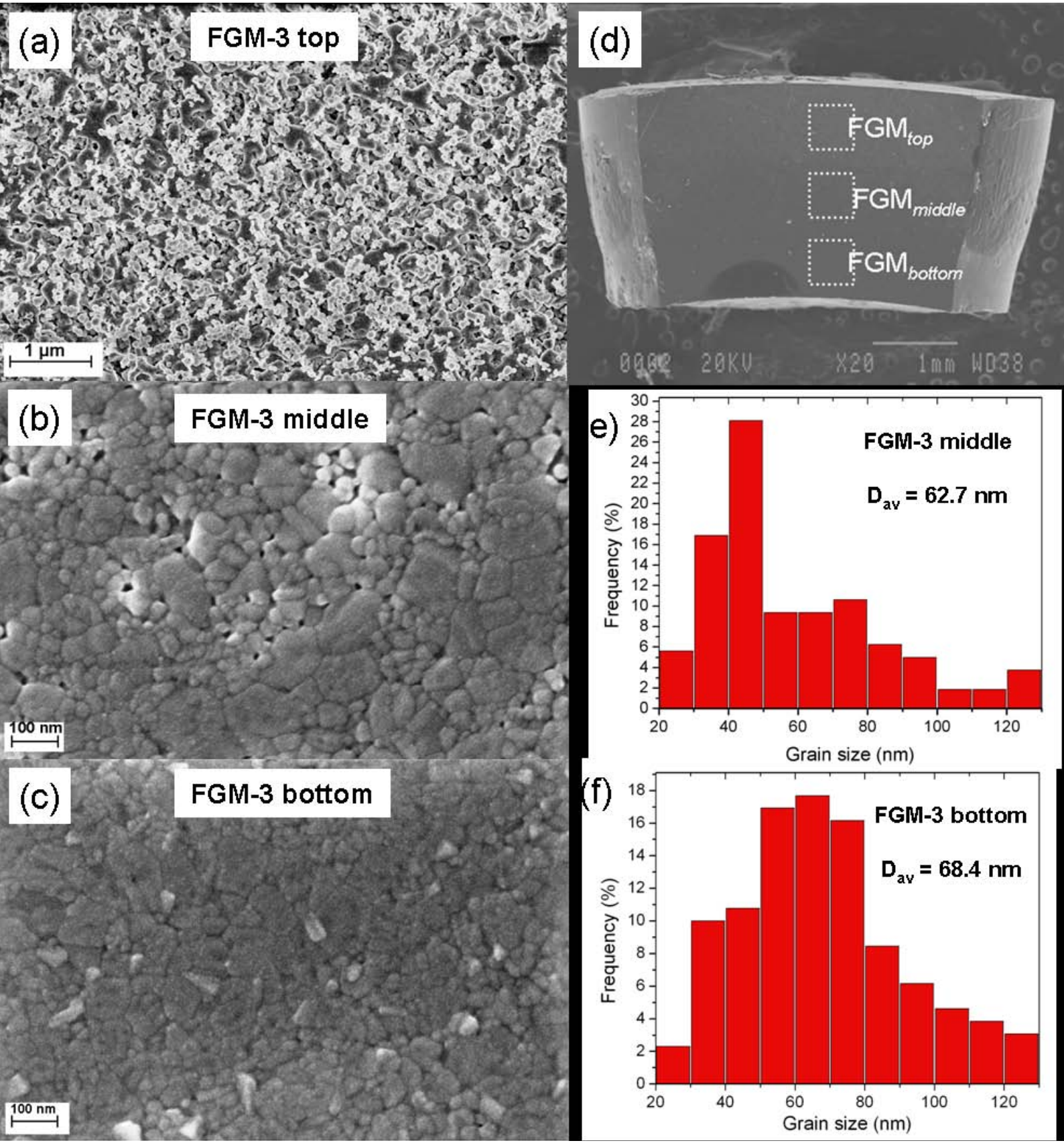
(a)
FGM-3 top
1 μm
(b)
FGM-3 middle
100 nm
(c)
FGM-3 bottom
100 nm
(d)
FGM$_{top}$
FGM$_{middle}$
FGM$_{bottom}$
20KV X20 1mm WD38
e)
FGM-3 middle
D_{av} = 62.7 nm
Frequency (%)
Grain size (nm)
(f)
FGM-3 bottom
D_{av} = 68.4 nm
Frequency (%)
Grain size (nm)

Fig. 7

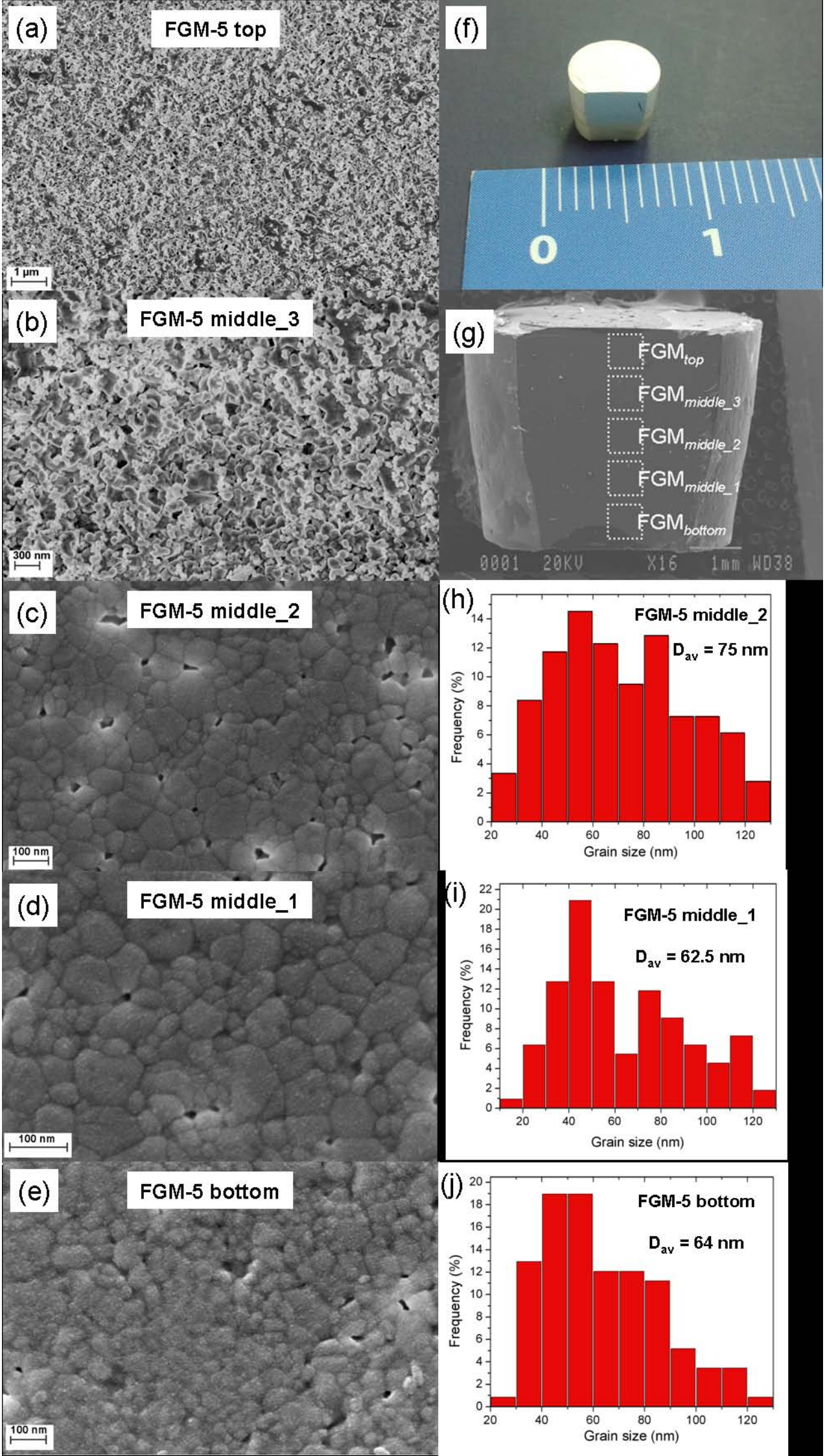
(a)
FGM-5 top
1 μm
(b)
FGM-5 middle_3
300 nm
(c)
FGM-5 middle_2
100 nm
(d)
FGM-5 middle_1
100 nm
(e)
FGM-5 bottom
100 nm
(f)
0
1
(g)
FGM$_{top}$
FGM$_{middle_3}$
FGM$_{middle_2}$
FGM$_{middle_1}$
FGM$_{bottom}$
0001 20KV X16 1mm WD38
(h)
FGM-5 middle_2
D_{av} = 75 nm
Frequency (%)
Grain size (nm)
(i)
FGM-5 middle_1
D_{av} = 62.5 nm
Frequency (%)
Grain size (nm)
(j)
FGM-5 bottom
D_{av} = 64 nm
Frequency (%)
Grain size (nm)

Fig. 8

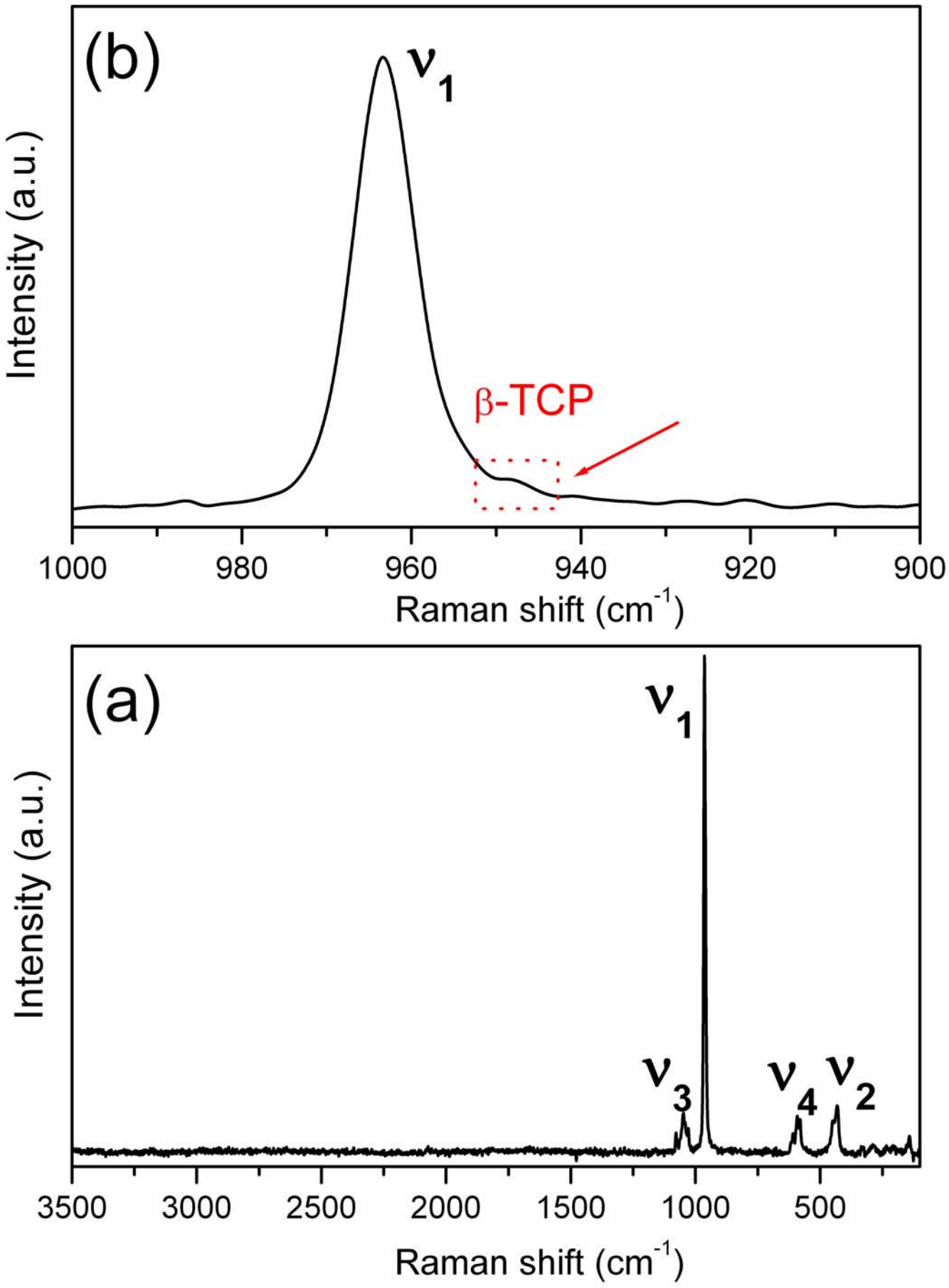
(b)
ν1
β-TCP
Intensity (a.u.)
1000
980
960
940
920
900
Raman shift (cm-1)
(a)
ν1
ν3
ν4
ν2
Intensity (a.u.)
3500
3000
2500
2000
1500
1000
500
Raman shift (cm-1)

Fig. 9

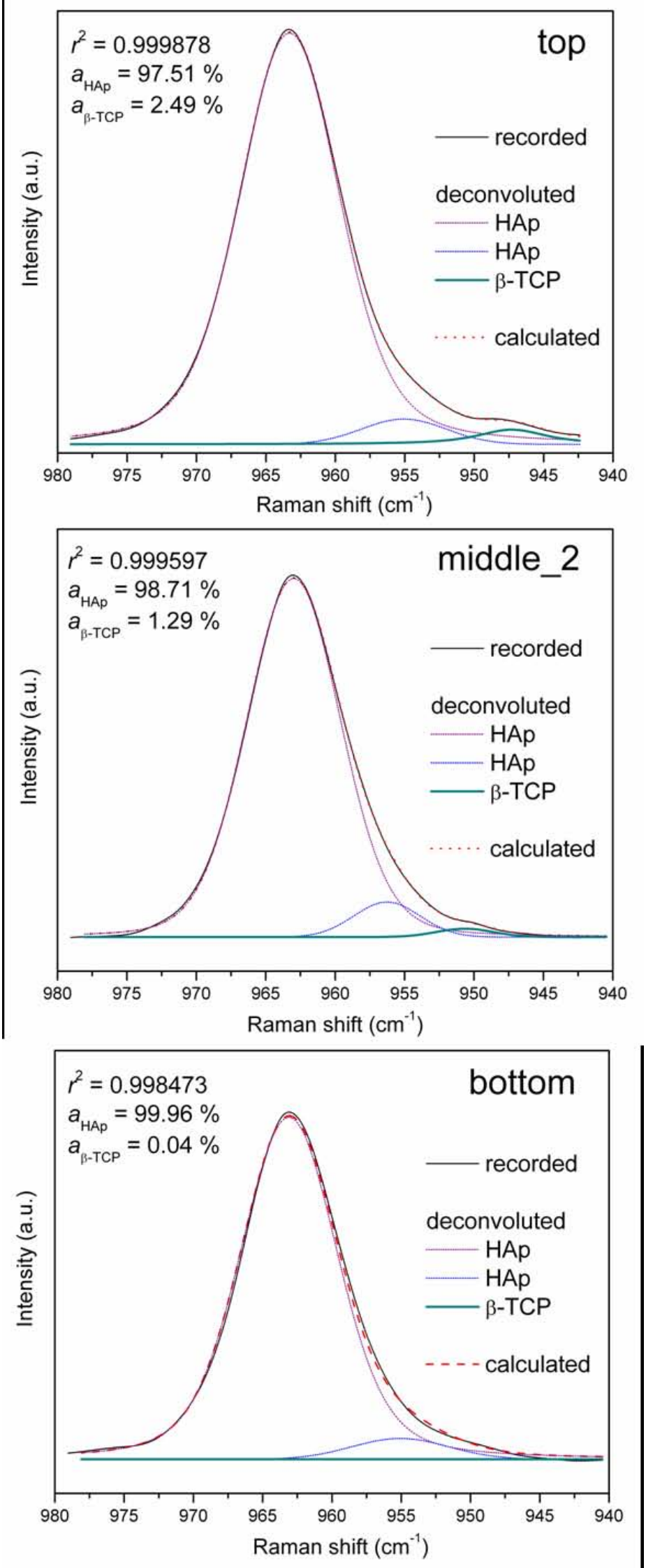
top
r^2 = 0.999878
a_{HAp} = 97.51 %
$a_{\beta\text{-TCP}}$ = 2.49 %
recorded
deconvoluted
HAp
HAp
β-TCP
calculated
Intensity (a.u.)
Raman shift (cm^{-1})
middle_2
r^2 = 0.999597
a_{HAp} = 98.71 %
$a_{\beta\text{-TCP}}$ = 1.29 %
recorded
deconvoluted
HAp
HAp
β-TCP
calculated
Intensity (a.u.)
Raman shift (cm^{-1})
bottom
r^2 = 0.998473
a_{HAp} = 99.96 %
$a_{\beta\text{-TCP}}$ = 0.04 %
recorded
deconvoluted
HAp
HAp
β-TCP
calculated
Intensity (a.u.)
Raman shift (cm^{-1})
980
975
970
965
960
955
950
945
940

Fig. 10

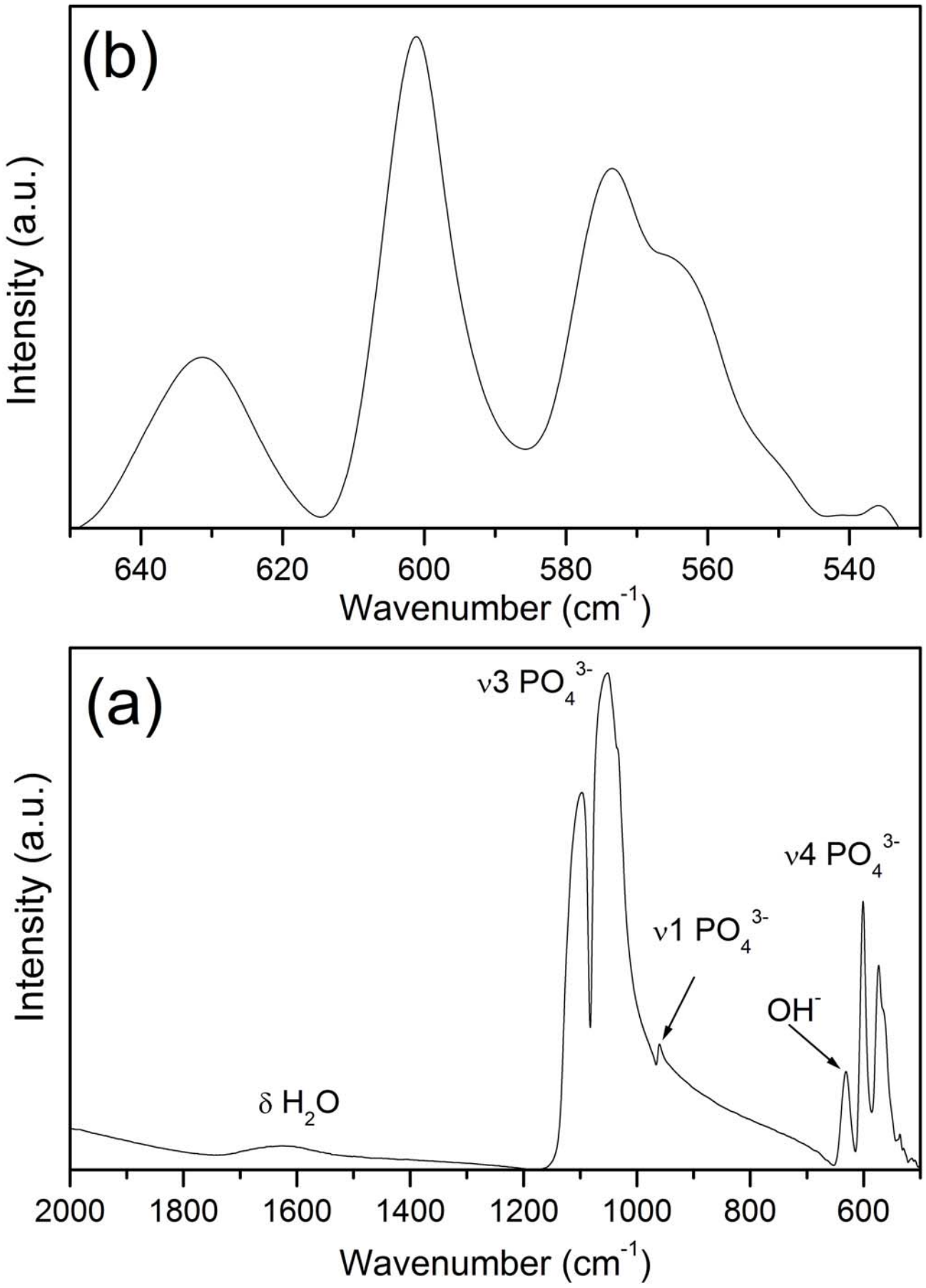
(b)
Intensity (a.u.)
640
620
600
580
560
540
Wavenumber (cm-1)
(a)
ν3 PO4 3-
ν4 PO4 3-
ν1 PO4 3-
OH-
δ H2O
Intensity (a.u.)
2000
1800
1600
1400
1200
1000
800
600
Wavenumber (cm-1)

Fig. 11

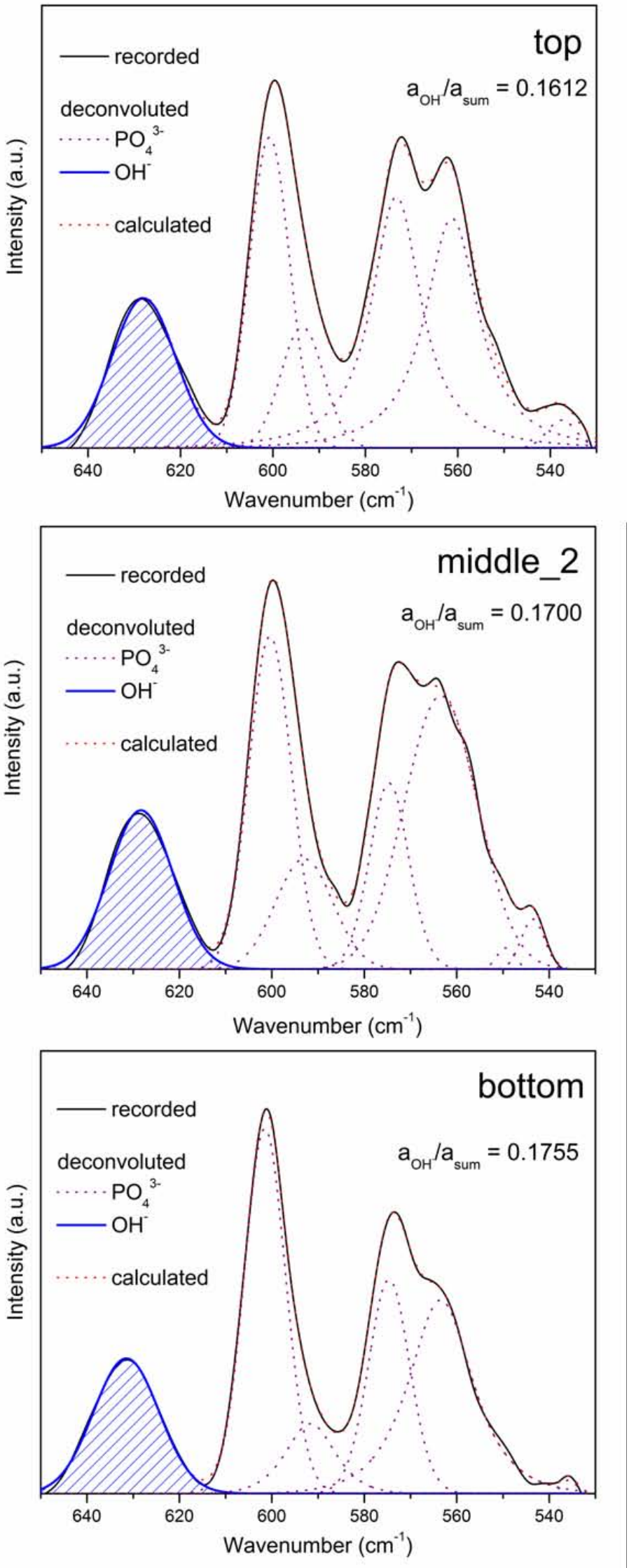
top
recorded
deconvoluted
PO4 3-
OH-
calculated
aOH/asum = 0.1612
Intensity (a.u.)
640
620
600
580
560
540
Wavenumber (cm-1)
middle_2
recorded
deconvoluted
PO4 3-
OH-
calculated
aOH/asum = 0.1700
Intensity (a.u.)
640
620
600
580
560
540
Wavenumber (cm-1)
bottom
recorded
deconvoluted
PO4 3-
OH-
calculated
aOH/asum = 0.1755
Intensity (a.u.)
640
620
600
580
560
540
Wavenumber (cm-1)

Fig. 12

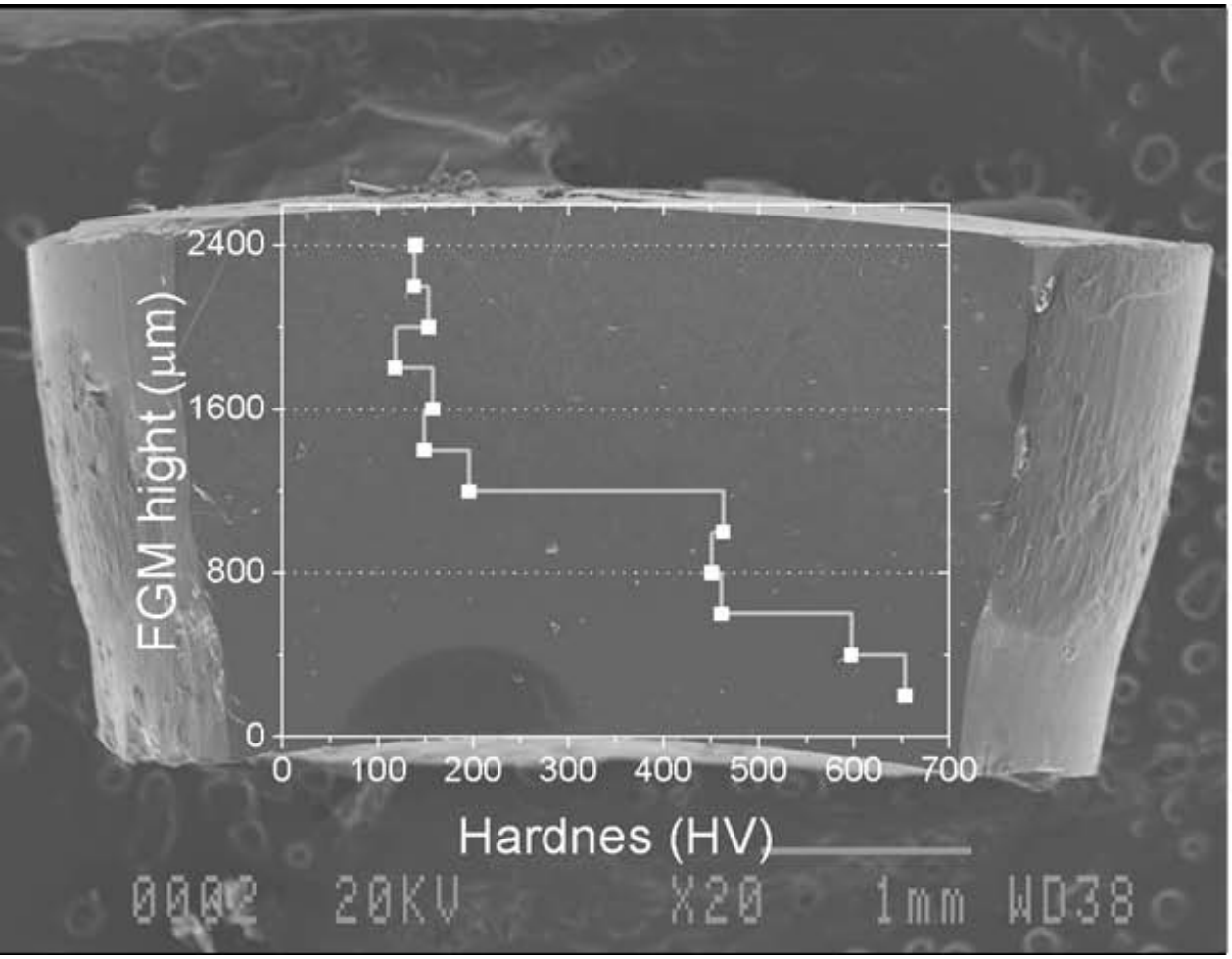
FGM hight (μm)
2400
1600
800
0
0
100
200
300
400
500
600
700
Hardnes (HV)
0002 20KV X20 1mm WD38

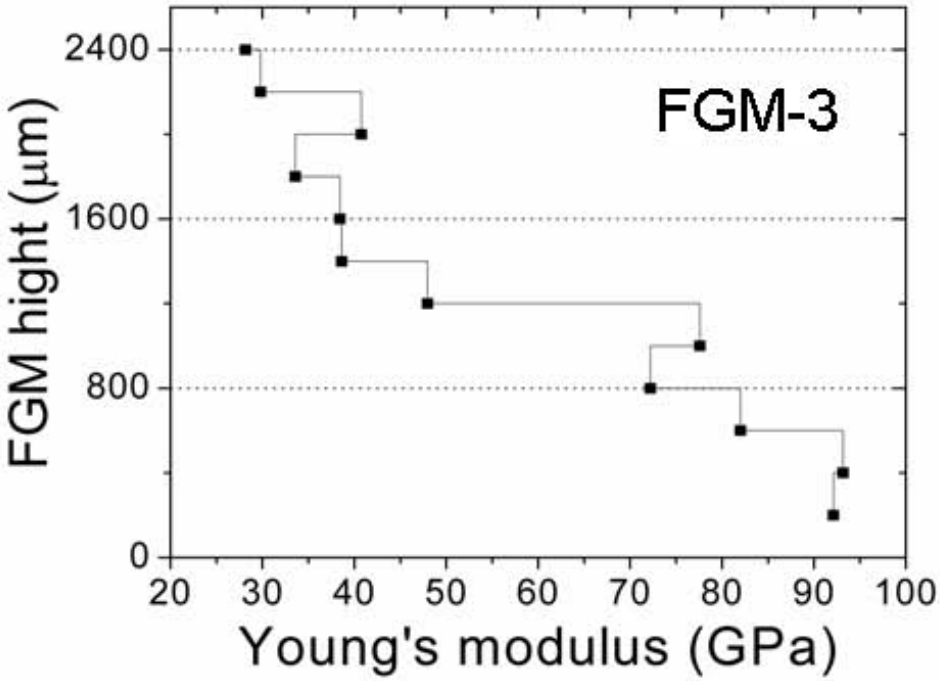
FGM-3
FGM hight (μm)
2400
1600
800
0
20
30
40
50
60
70
80
90
100
Young's modulus (GPa)

Fig. 13

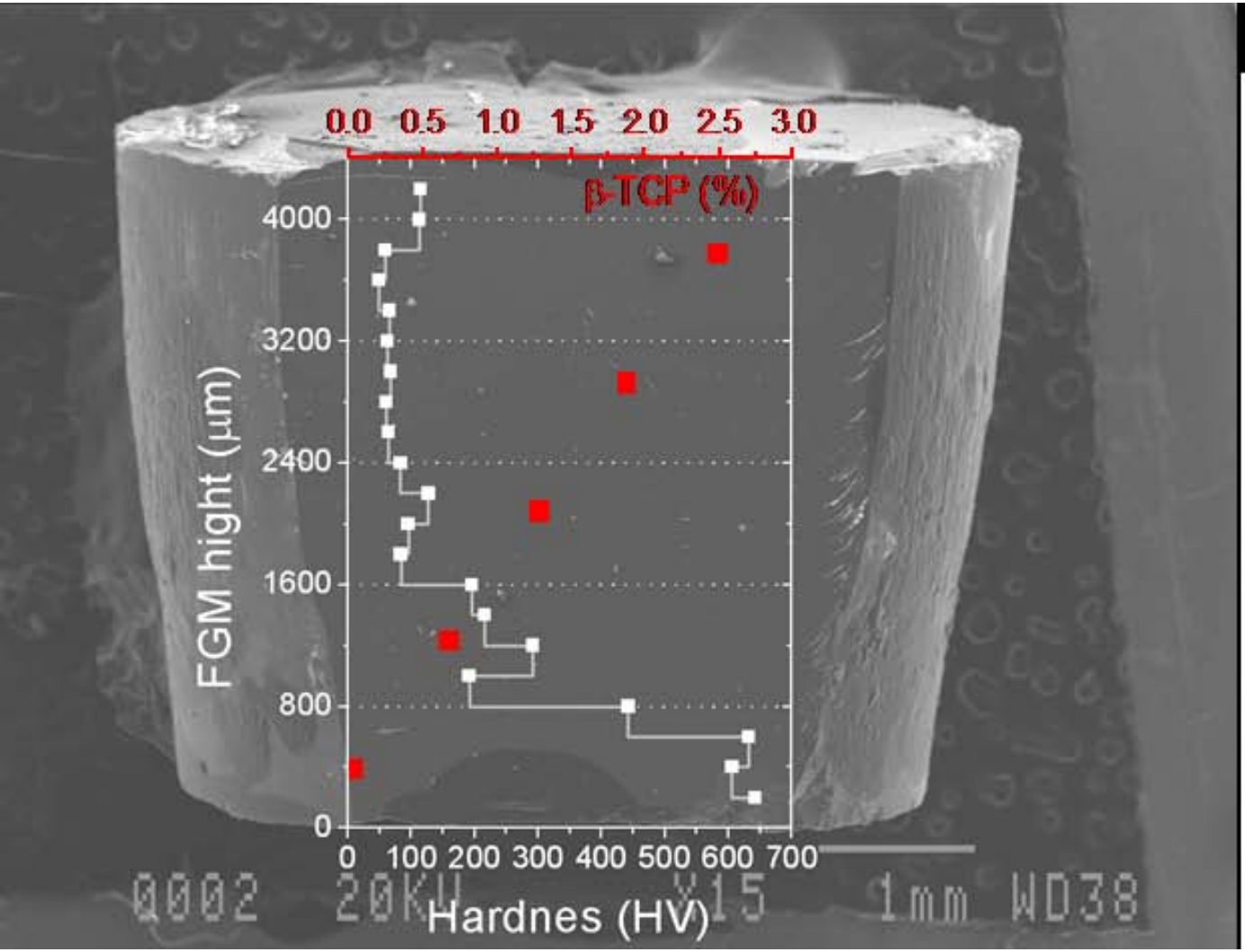
0.0 0.5 1.0 1.5 2.0 2.5 3.0
β-TCP (%)
FGM hight (μm)
4000
3200
2400
1600
800
0
0 100 200 300 400 500 600 700
Hardnes (HV)
Q002 20KV V15 1mm WD38

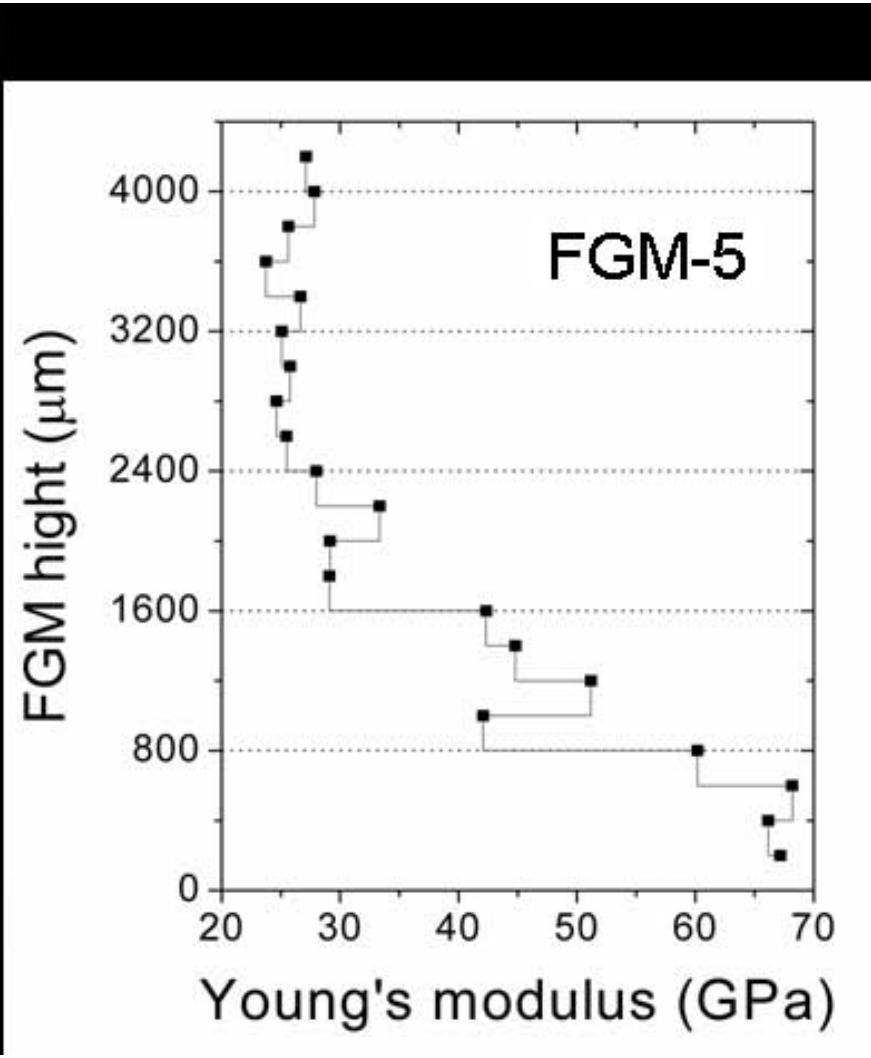
FGM-5
FGM hight (μm)
4000
3200
2400
1600
800
0
20 30 40 50 60 70
Young's modulus (GPa)